Enhanced iceberg discharge in the western North Atlantic during all Heinrich events of the last glaciation

Yuxin Zhou [a,b,*], Jerry F. McManus [a,b], Allison W. Jacobel [a,b,1], Kassandra M. Costa [a,b,2], Shouyi Wang [a,b,2], Blanca Alvarez Caraveo [a,b,3]

[a] *Lamont-Doherty Earth Observatory of Columbia University, Palisades, NY 10964, USA*
[b] *Dept. of Earth and Environmental Sciences, Columbia University, New York, NY 10027, USA*

A R T I C L E   I N F O

A B S T R A C T

A series of catastrophic iceberg and meltwater discharges to the North Atlantic, termed Heinrich events, punctuated the last ice age. During Heinrich events, coarse terrigenous debris released from the drifting icebergs was preserved in deep-sea sediments, serving as an indicator of iceberg passage. Quantifying the vertical flux of ice-rafted debris (IRD) in open-ocean settings can resolve questions regarding the timing and spatial variation in ice sheet calving intensity. In this study, $^{230}Th_{xs}$-based IRD flux throughout the last glacial period was measured in a deep-sea sediment core from the western North Atlantic, and complemented by data spanning 0-32 ka from a sediment core in the Labrador Sea. The cores were recovered from sites downstream from Hudson Strait, a likely conduit for icebergs calving from the Laurentide ice sheet (LIS). We compare our results with equivalent existing data from the eastern North Atlantic and show that the two cores in our study have higher IRD fluxes during all Heinrich events, notably including events H3 ($\sim$31 ka) and H6 ($\sim$60 ka). This study demonstrates that the LIS played a role in all Heinrich events, and raises the likelihood that a single mechanism can account for the genesis of these events.

1. Introduction

During the last glacial period, the classic Greenland ice core records document Dansgaard-Oeschger (D-O) events, rapid shifts in air temperature over the ice cap of $\sim$8 °C within a few decades (NGRIP members, 2004 and references therein). Throughout the same interval, subpolar North Atlantic deep-sea sediments preserve evidence of century-scale episodes of catastrophic iceberg and meltwater discharge known as Heinrich events (HEs). Sedimentary evidence of meltwater discharges coeval with HEs has also been documented in the Labrador Sea (e.g., Andrews, 1998; Hesse, 2016). The passage of icebergs is marked by ice-rafted debris (IRD), which forms layers rich in detrital material within glacial sediment sequences (Hemming, 2004 and references therein).

The icebergs discharged during HEs drifted and melted across the subpolar North Atlantic Ocean, an important region of deep-water formation that is sensitive to disruption by surface water freshening (Ganopolski and Rahmstorf, 2001 and references therein). Indeed, the freshwater flux associated with these events is thought to have dramatically and repeatedly weakened the Atlantic Meridional Overturning Circulation (AMOC) (Henry et al., 2016; Hughen et al., 2004; McManus et al., 2004). Alternatively, subsurface warming has been proposed as a mechanism that can destabilize the LIS substantially to produce the significant calving events (e.g., Bassis et al., 2017). During HEs, the Northern Hemisphere cooled (Dansgaard et al., 1993) while the Southern Hemisphere warmed (EPICA Community Members, 2006). The oceans, cryosphere, and atmosphere all interact in connected ways during HEs, making these events ideal targets for examining how abrupt climate change unfolds.

An unsolved mystery of HEs is the apparently anomalous behavior associated with H3 ($\sim$31 ka) and H6 ($\sim$60 ka). These two events are often regarded as atypical because of their relatively low IRD concentrations and the absence of detrital carbonates in the eastern subpolar North Atlantic (Broecker et al., 1992). In this

---

* Corresponding author at: Lamont-Doherty Earth Observatory of Columbia University, Palisades, NY 10964, USA.

E-mail address: yzhou@ldeo.columbia.edu (Y. Zhou).

[1] Now at Dept. of Geology, Middlebury College, Middlebury, VT 05753, USA and Dept. of Earth, Environmental, and Planetary Sciences, Brown University, Providence, RI 02912, USA.

[2] Now at Dept. of Geology and Geophysics, Woods Hole Oceanographic Institution, Woods Hole, MA 02543, USA.

[3] Now at Dept. of Atmospheric and Oceanic Sciences, University of California, Los Angeles, Los Angeles, CA 90095, USA.

paper, we will refer to the other HEs, H1, H2, H4, and H5, as the "typical" HEs and H3 and H6 as "atypical." The observed differences between the typical and the atypical events have alternatively been explained by the variable behavior of the ocean or the cryosphere. From a glaciological perspective, the provenance of IRD and the rate of climate change during the atypical events suggests a European ice sheet origin that led to smaller iceberg fluxes in the western North Atlantic (e.g., Bigg et al., 2011), although this claim has been disputed (Jullien et al., 2006). A complementary hypothesis suggests that H3 and H6 occurred at the onset of Marine Isotope Stage (MIS) 2 and MIS4 when the LIS was just starting to grow, resulting in a smaller magnitude of calving and meltwater release (Gwiazda et al., 1996). From an oceanographic perspective, assuming that all the events originated from the LIS, warmer sea-surface temperatures might have melted the icebergs closer to their western source during the two atypical HEs (Bond et al., 1992). Consistent with that view, Pb isotope data suggest that, in the eastern North Atlantic, the relatively IRD-rich layers are actually the results of foraminifera-dissolution events (Gwiazda et al., 1996). The lack of foraminifera in these layers would cause an apparent increase in the proportion of IRD, the other major coarse constituent in North Atlantic sediments. The robustness of these divergent observations is relevant to understanding the mechanism(s) accounting for these dramatic events. Similar behavior of the events would fit more readily into a single mechanism, while contrasting behavior suggests different, even drastically divergent, mechanisms or forcing at different times.

Reconstructing the IRD deposition rate provides a straightforward test of these competing hypotheses. This was done previously in broad temporal ranges (Ruddiman, 1977). If the increased IRD concentrations in H3 and H6 are solely the result of foraminifera dissolution, the IRD fluxes (deposition rate per unit area per unit time) during these periods should not increase. If the icebergs that originated in the west melted at a higher rate during the atypical HEs, the IRD fluxes would have been higher in the west than the east. The atypical HE IRD fluxes might also have been even higher than during the typical HEs at the western sites, assuming the total magnitude of calving remained the same. If the increases in Laurentide ice sheet calving were smaller during the atypical HEs than the typical HEs, or if the iceberg IRD concentration was lower, the IRD fluxes would have shown a visible but smaller increase above ambient glacial deposition than the typical HEs throughout the basin. Lastly, if the two atypical events did originate from the European ice sheet, or if the iceberg melting rate decreased such that the majority of the icebergs melted in the east, or if the IRD was distributed differently within the icebergs and released in a later stage of melting, the IRD fluxes in the east should have been higher than the west.

Quantifying IRD fluxes during HEs provides a way to test the various aforementioned hypotheses regarding the two atypical events. This hypothesis-testing can be achieved with ^{230}Th normalization. The rapid scavenging of ^{230}Th results in a near balance between its burial and local production, allowing it to be used to reconstruct vertical mass flux (Costa et al., 2020). The scavenging of ^{230}Th is insensitive to the proportion of lithogenic and carbonate material in the sediments (Chase et al., 2002). IRD flux can therefore be reconstructed from the ^{230}Th-normalized burial flux of sediment that is uniquely identified as IRD (McManus et al., 1998).

Previously, century-scale measurements of IRD flux have only been made in the eastern North Atlantic (McManus et al., 1998). Here we present a 135-thousand-year (kyr) record of ice-rafted debris flux from a location off the coast of Newfoundland, 2200 km downstream from the Hudson Strait. We complement it with a record from Orphan Knoll, also off the coast of Newfoundland, that is ~1700 km downstream from the Hudson Strait and ex-

tends through H3. By comparing our ice-rafting flux records with the directly equivalent existing data in the eastern North Atlantic (McManus et al., 1998), we demonstrate that H3 and H6 are mechanistically consistent with the other HEs of the last glaciation. This project resolves longstanding uncertainties and simplifies our understanding of these events.

2. Methods

EW9303-37JPC (43.68°N, 46.28°W, 3981 m, IGSN: DSR000507, JPC37 hereafter) is a 13.3 m long jumbo piston core retrieved at the foot of a continental slope off the coast of Newfoundland, Canada (Fig. 1). DY081-GVY001 (50°09'36"N, 45°30'36"W, 3721 m, GVY001 hereafter) is a 5.1 m long gravity core retrieved near Orphan Knoll (Hendry et al., 2019). Both sites are presently under the influence of the surficial Labrador Current, which transports icebergs southward in the Labrador Sea. At depth, the deep western boundary current (DWBC) also flows southward past the sites (McCartney, 1992).

Samples of 8-10 g were taken at 2 cm intervals from JPC37, and at 5 cm intervals from GVY001, then freeze dried, weighed, and washed through 63 μm sieves to separate coarse and fine fractions. The proportion of coarse sediment (%coarse) was calculated by dividing the dried >63 μm fraction weight by the total dry weight. Subsequently, the coarse fraction was dry-sieved at >150 μm and split so that 300-400 foraminifera shells and ~100 IRD grains could be identified and counted under a microscope. We note that although we use >150 μm as representative of the IRD presence, other studies use different size thresholds (Andrews and Voelker, 2018). Foraminifera counts were used to calculate the relative abundance of the polar planktic foraminifera, *Neogloboquadrina pachyderma* (hereafter *N. pachy.*), calculated as the number of *N. pachy.* specimens in a sample divided by the total number of planktic foraminifera shells. The relative abundance of IRD (hereafter %IRD) was calculated as the number of IRD grains divided by the sum of IRD grains plus planktic foraminifera shells.

During microscope counting work, eight to ten specimens of *N. pachy.* were picked for δ^{18}O and δ^{13}C analysis in the Lamont-Doherty Earth Observatory of Columbia University (LDEO) stable isotope laboratory, using a Thermo Delta V Plus equipped with a Kiel IV individual acid-bath sample preparation device. Measurements made on standard carbonate NBS19 yield a standard deviation of 0.06‰ for δ^{18}O and 0.03‰ for δ^{13}C.

Elemental intensities from JPC37 were measured using an X-ray fluorescence (XRF) core scanner (ITRAX, Cox Ltd., Sweden) at LDEO at 2 mm resolution, using an integration time of 10 s and a molybdenum x-ray source set to 30 kV and 50 mA. The intensities were calibrated with flux fusion concentration measurements from JPC37, following the procedure of Murray et al. (2000). Sediment samples spanning the range of XRF intensities were randomized, interspersed with standard reference materials (e.g., JLS-1, JDO-1, SCO-1, AGV-2, DTS-2b, W-2a), ashed, digested in HF and HNO$_3$ overnight, and diluted for analysis on an Agilent 720 Inductively Coupled Plasma Optical Emission Spectrometer (ICP-OES) at LDEO. The ICP-OES data provide a robust calibration ($R^2 = 0.80$ for Ca, $R^2 = 0.90$ for Sr) for the high-resolution XRF records. Elemental intensities from GVY001 were measured from a similar ITRAX XRF core scanner at the British Ocean Sediment Core Research Facility (BOSCORF; Hendry et al., 2019). The elemental intensities from GVY001 are uncalibrated and presented as ratios.

Bulk wet density and magnetic susceptibility from JPC37 were obtained at 1 cm resolution from a Geotek multi-sensor core logger at the Lamont-Doherty Core Repository. Local anomalously low-density peaks were identified as cracks formed due to drying and omitted in data processing. Bulk wet density and magnetic sus-
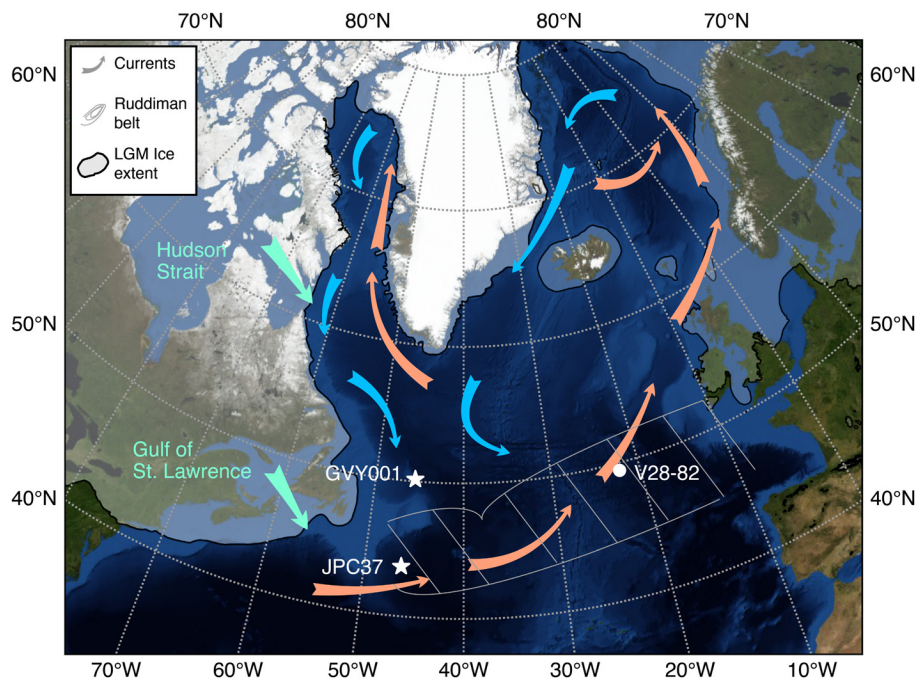
Fig. 1. North Atlantic map with core locations. Stars depict the locations of cores used by this study: JPC37 (43°58'N, 46°25'W, 3981 m); GVY001 (50°09'36"N, 45°30'36"W, 3721 m). The white dot is the core used for comparison of IRD flux: V28-82 (49°27'N, 22°16'W, 3935 m) (McManus et al., 1998). The frosted area represents ice sheet extent during the Last Glacial Maximum (Ehlers et al., 2011). Red and blue arrows are the warm and cold surface circulation, respectively, after (Hemming et al., 2002). Aqua arrow leaving the Hudson Strait represents the calving of icebergs from the LIS. Aqua arrow leaving the Gulf of St. Lawrence denotes additional calving of icebergs that could influence JPC37. Hashed area delineates the Ruddiman IRD belt (Ruddiman, 1977). Basemap from NASA Blue Marble June image (Stockli et al., 2005). (For interpretation of the colors in the figure(s), the reader is referred to the web version of this article.)

ceptibility from GVY001 were obtained at 1 cm resolution from a similar Geotek instrument at BOSCORF.

Each bulk sediment sample of ~100 mg was spiked, digested (Fleisher and Anderson, 1991), purified, and analyzed for uranium and thorium isotope activities. The last step was done on an Element Plus inductively coupled plasma mass spectrometer (ICP-MS) at LDEO. The conversion from raw counting data to activities and associated error propagation has been packaged into a Python script named ThxsPy accessible at https://github.com/yz3062/ThxsPy.

Sediment fluxes were calculated using $^{230}Th_{xs}$, which is the ^{230}Th derived from the decay of ^{234}U in seawater and subsequently scavenged by adsorption onto settling particles (Bacon and Anderson, 1982). To calculate $^{230}Thxs$, other sources of non-excess ^{230}Th need to be quantified and removed (Costa et al., 2020 and references therein).

Detrital ^{230}Th is the ^{230}Th produced from the radioactive decay of ^{238}U in mineral lattices. Detrital ^{238}U can be estimated by assuming a constant detrital $^{238}U/^{232}Th$ and that all measured ^{232}Th is detrital. A range of $(^{238}U/^{232}Th)_{detrital}$ between 0.47 and 0.7 has been used by previous studies in this region (Table S1). We conducted a leaching experiment in JPC37 to isolate the detrital uranium and thorium and determined $(^{238}U/^{232}Th)_{detrital}$ to be 0.48. We further determined from the leaching experiment the disequilibrium in $(^{230}Th/^{238}U)_{detrital}$ caused by α recoil to be 0.81 (details in Discussion).

The radioactive decay of ^{238}U that precipitated from the soluble form U(VI) to its insoluble form U(IV) in anoxic, reducing sediments produces ^{230}Th (Barnes and Cochran, 1990). Assuming the non-detrital portion of ^{238}U is authigenic, the derived ^{230}Th (abbreviated to authigenic ^{230}Th) can be calculated using a seawater $^{234}U/^{238}U$ of 1.1468 (Andersen et al., 2010) and applying the classic radio-decay equations.

In summary, the calculation of $^{230}Th_{xs}$ is thus

$$^{230}Th_{xs} = {}^{230}Th_{measured} - {}^{230}Th_{detrital} - {}^{230}Th_{authigenic}$$
$$= {}^{230}Th_{measured} - (^{238}U/^{232}Th)_{detrital} * (^{230}Th/^{238}U)_{detrital} * {}^{232}Th_{measured} - (^{238}U_{measured} - (^{238}U/^{232}Th)_{detrital} * (^{230}Th/^{238}U)_{detrital} * {}^{232}Th_{measured}) * [(1-e^{-\lambda 230*t}) + \lambda_{230}/(\lambda_{230}-\lambda_{234})(e^{-\lambda 234*t} - e^{-\lambda 230*t})((^{234}U/^{238}U)_{seawater}-1)]$$

Where $(^{238}U/^{232}Th)_{detrital}$ is 0.48, $(^{230}Th/^{238}U)_{detrital}$ is 0.81, λ is the isotope decay constant, $(^{234}U/^{238}U)_{seawater}$ is 1.1468, and t is the time of decay since deposition.

The values of $(^{238}U/^{232}Th)_{detrital}$ and $(^{230}Th/^{238}U)_{detrital}$ used by this study are different from most previous studies and are based on experimental results (Table S1). We conducted leaching experiments throughout core JPC37 to obtain representative lattice-bound isotopic ratios. Bulk samples were leached with 5 mL of 1N or 3N HCl and sonicated for 20 min. After a 5 min centrifuge, the supernatant was decanted. In some cases, the supernatant was filtered using 0.42 μm filters. The rest of the procedure is the same as described above for typical sediment U-Th analysis. The strength of acid and time of sonication used were shown previously to remove authigenic uranium effectively without leaching lattice-bound uranium and thorium (Robinson et al., 2008).

From $^{230}Th_{xs}$, we can calculate the vertical mass flux

$$F = \beta * Z/^{230}Th_{xs,0}$$

Where F is the vertical mass flux, β is the production rate of ^{230}Th, Z is the water depth, and $^{230}Th_{xs,0}$ is $^{230}Th_{xs}$ corrected for decay since deposition using the independent age model. Everywhere else in this paper, we use $^{230}Th_{xs}$ as a shorthand of $^{230}Th_{xs,0}$. We can further calculate the IRD flux

$$IRD\ flux = F * \#IRD\ /\ M$$

where #IRD is the total number of IRD grains, and M is the dry bulk mass.
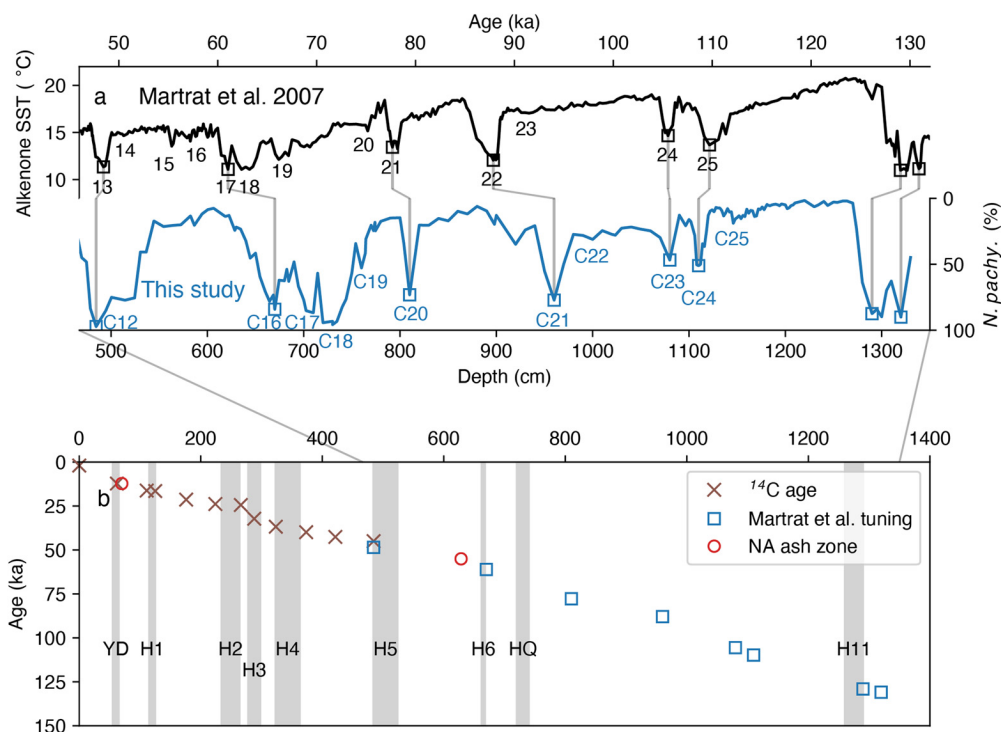
Fig. 2. Chronology of JPC37. Variations in *N. pachy.* relative abundance are correlated with an alkenone unsaturation SST record (Martrat et al., 2007; Iberian margin stadials marked in black numbers) (a). That SST record was previously tied to the North Greenland Ice Core Project (NGRIP) chronology. Blue numbers denote cooling events (McManus et al., 2002, 1994; see Fig. S7 for details). Tie points to our core are marked by thin gray lines. The lower panel contains the compilation of all age control points, including radiocarbon dating, tephrochronology, and tuning with alkenone record (b).

3. Chronology

The chronology of JPC37 from modern to ∼46 ka is based on radiocarbon dating. Monospecific samples of 350-400 specimens of *N. pachy.*, the most abundant foraminifera species in this core, were picked from the >150 μm fraction. These foraminifera shells were sonicated in water and ethanol to remove any fine-grained sediment, including detrital carbonate that can potentially bias the results. Radiocarbon analyses were performed at the NOSAMS-WHOI facility (see Appendix A for a link to data). The calibration to calendar ages uses Marine 20 (Heaton et al., 2020) and the CALIB program (Stuiver et al., 2021), with a standard 550 yr marine reservoir correction. Past changes in marine reservoir ages are uncertain (Heaton et al., 2020) but not to the extent as to influence our identification of HEs.

The chronology of JPC37 beyond the range of radiocarbon is determined by aligning our %*N. pachy.* with an alkenone-based sea-surface temperatures (SST) record from MD01-2444 (Martrat et al., 2007; Fig. 2a). The polar foraminifera *N. pachy.* lives in the coldest environment among planktic species and its abundance in JPC37 signals low SST (Ericson, 1959). MD01-2444 (37°33.68′N, 10°08.53′W, 2637 m) is on the Iberian margin and its latitude is comparable to JPC37. Its chronology is based on temperature alignment with the North Greenland Ice Sheet Project (NGRIP) ice core during the last glacial (NGRIP members, 2004) and before that, Antarctica Dome C (EPICA Community Members, 2004). Even though the two sites sit on the opposite side of the North Atlantic basin, the prevailing westerlies and the resulting current put MD01-2444 downstream from JPC37. As a result, the temperatures at the two sites should be closely correlated during regional-scale climate changes. The uncertainties associated with the MD01-2444 age model are propagated to our chronology as well.

The core chronology of JPC37 is corroborated with tephrochronology. We found several concentrated zones of plates of glassy, bubble-wall shards, consistent with the description of Ruddiman

and Glover (1972). The shards are mostly non-existent outside of the zones. The youngest of these zones, at 70 cm, is identified as Ash Zone 1. The commonly assumed age of Ash Zone 1 (12.2 cal ka BP) (Andrews and Voelker, 2018) is only 700 yrs apart from the radiocarbon-based age model. Ash Zone 2 is identified at 628.5 cm and was previously dated to 55.4 ka in the NGRIP record based on the GICC05 age model (Svensson et al., 2008) and 54.5 ka by Ar-Ar dating of the volcanic ash (Southon, 2004), whereas in our age model it is at 57.4 ka. Outside of these two zones, glass shard counts are also high at H3 and H6. We cannot rule out that the shards at Heinrich layer 3 were delivered by a gravity flow.

The chronology of GVY001 is based on radiocarbon and tephrochronology. Radiocarbon analysis (n=7) in this core follows the same procedure as in JPC37, except for the youngest sample at the depth of 2 cm. At that depth we used *G. bulloides* instead of *N. pachy.* since not enough *N. pachy.* were found. Although age offsets have been identified in co-occurring planktic species (e.g. Broecker et al., 1988), an offset of centuries or even millennia at this one horizon is not likely to alter our HE identification. Ash Zone 1 is identified at 58 cm, and we use 12.2 ka BP as its age (Andrews and Voelker, 2018).

4. Results

The age models indicate average sedimentation rates in both cores are moderately high: ∼10 cm/kyr in JPC37 and ∼12 cm/kyr in GVY001 (Fig. 2 and Fig. S1). Core JPC37 captured the whole last glacial-interglacial cycle (MIS 1-5) and the very end of MIS 6, whereas core GVY001 extends to just beyond 30 ka. Crossed beddings of foraminifera-rich sands are found in JPC37 around depths 288 cm – near the depth where H3 is found (Fig. S2) – and 1312 cm. These sands are likely caused by turbidites and could influence the interpretation of results from this particular interval. Data from H3 in JPC37 is therefore considered tentative except when it
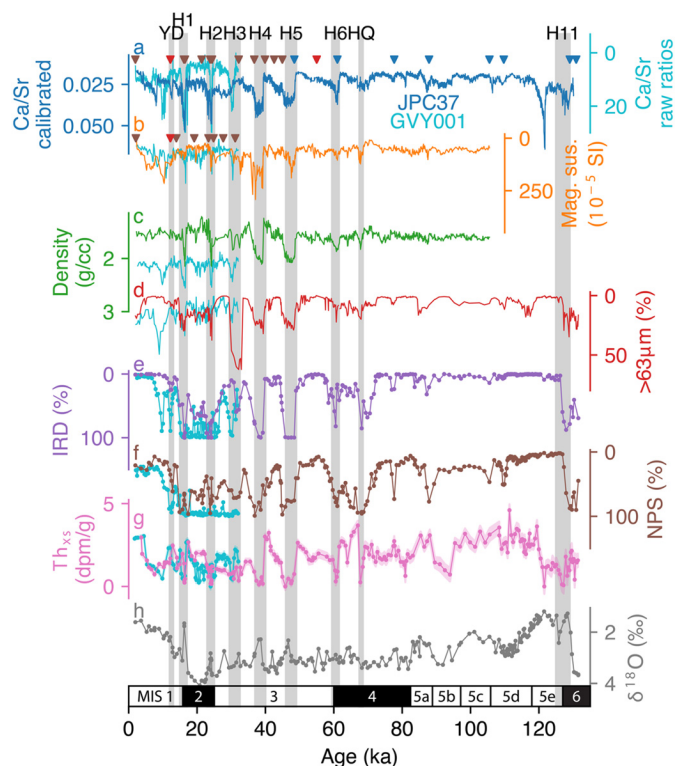
Fig. 3. GVY001 (cyan) and JPC37 (other colors) Ca/Sr with JPC37 age control points marked by red (ash zone), brown (radiocarbon), and blue (SST tie points) triangles (a), magnetic susceptibility with GVY001 age control point marked by red (ash zone) and brown (radiocarbon) triangles (b), bulk wet sediment density (c), coarse (>63 μm) fraction (d), IRD abundance (e), *N. pachy.* abundance, of which the early last interglacial (95-125 ka) data are partially from McManus et al. (2002) (f), $^{230}Th_{xs}$ with shading marking 2σ uncertainty (g), and *N. pachy.* $\delta^{18}O$ (h). Gray bars are Younger Dryas (YD), H1-6, H11, as well as HQ, as predicted by Bassis et al. (2017).

is supported by independent evidence from GVY001, which is from a different location not influenced by any turbidite deposits.

In JPC37, %IRD varies between 0% and 100% (Fig. 3e). At five depths, %IRD reached 100%. At three other depths, %IRD reached 50%. The majority of the %IRD peaks are found in the upper (glacial) part of the core. Heinrich layers are identified by peaks in %IRD, as well as peaks of Ca/Sr that are indicative of detrital carbonate (Hodell et al., 2008), magnetic susceptibility, density, and %coarse (Fig. 3). Layers with prominent increases in all of these proxies are present in MIS 2-4 and late MIS 6. H4 and H5 show the strongest signals in all of these proxies, consistent with previous findings (Hemming, 2004). Several episodes of smaller magnitude in all of the proxies can be found during early MIS 5. The strongest peak of Ca/Sr appears at 1220 cm depth and is matched with a $^{230}Th_{xs}$ low. However, no signals in magnetic susceptibility, %coarse, %IRD, *N. pachy.*, or $\delta^{18}O$ are present at this depth (density data does not extend to this depth). This discrepancy suggests the delivery of fine detrital carbonates at a high rate without freshwater flux or lower SST. In GVY001, %IRD ranges between 0% and 100% (Fig. 3e). Compared to JPC37, %IRD in GVY001 is higher on average. Ca/Sr, magnetic susceptibility, density, and %coarse help identify HEs. Possibly due to GVY001's more poleward location and setting within the cold Labrador current, %IRD and *%N. pachy.* are saturated to 100% during most of the last glacial period.

In JPC37, *%N. pachy.* has a range between 1% and 99% (Fig. 3f). Peaks of *%N. pachy.* can be found at the same or slightly above the depths of %IRD peaks. $\delta^{18}O$ of *N. pachy.* ranges between 1.2‰ and 4.1‰ and displays a hybrid signal that combines the typical sawtooth glacial-interglacial pattern and episodes of depletion

corresponding to HEs. In each of the identified HEs, *%N. pachy.* increased while the $\delta^{18}O$ of *N. pachy.* decreased. During HEs, *%N. pachy.* continues to vary even when %IRD stabilizes at a high value.

Our leaching experiment on JPC37 sediments suggests that the recoil-related losses of ^{234}U and ^{230}Th are about 10% each on average in Heinrich layer detrital sediments and higher in between (Fig. S3). The variations in $^{234}U/^{238}U$ are smaller than those of $^{230}Th/^{234}U$. We use 0.9 for $^{230}Th/^{234}U$ and $^{234}U/^{238}U$ and 0.81 for $^{230}Th/^{238}U$ for both cores. The leaching experiment also suggests a potentially broad range in the detrital $^{238}U/^{232}Th$ ratio (Fig. S4), but the five leaching experiments made in Heinrich layer 4 have an average of 0.48, which we use in this study.

The $^{230}Th_{xs}$ profile from JPC37 contains values that vary between 0-5 dpm/g. Low $^{230}Th_{xs}$ values (<0.5 dpm/g) are observed at 16.3, 24.0, 38.1, 45.8, 60.6, and 67.8 ka during the last glacial period. The low $^{230}Th_{xs}$ episodes have ages one thousand years within the previously determined HE ages (Hemming, 2004), which is broadly within the uncertainty of radiocarbon dating. One sample in H4 and another in late MIS 6 have $^{230}Th_{xs}$ so low that their 95% uncertainty ranges barely reach above 0. GVY001 resembles JPC37 in $^{230}Th_{xs}$ for the most part, except the periods before and after H2.

In JPC37, mass fluxes range between 2 g/cm^2 kyr and 133 g/cm^2 kyr, although higher mass fluxes are associated with higher uncertainties. There are nine peaks of mass flux. Outside of the mass flux peaks, mass flux fluctuates around 4 g/cm^2 kyr. IRD flux varies between 1 grain/cm^2 kyr and 560,000 grains/cm^2 kyr. At eight depth ranges, the values of IRD flux reach above 50,000 grains/cm^2 kyr. These depths coincide with HEs. The IRD fluxes during H5 and H11 are the highest among HEs, with values at or above 500,000 grains/cm^2 kyr. The IRD fluxes during H2 and H4 are around 250,000 grains/cm^2 kyr. The IRD fluxes at H1, H6, and the event prior to H6 are lower at 100,000 grains/cm^2 kyr, 41,000 grains/cm^2 kyr, and 42,000 grains/cm^2 kyr, respectively. The IRD fluxes during each HE and the event prior to H6 are statistically distinct from the ambient IRD flux, even at the smallest event (H6), where the p-value of the "Student's" t-Test is 4×10^{-6}. In GVY001, mass flux ranges from 3 g/cm^2 kyr to 40 g/cm^2 kyr. The peaks of mass flux at GVY001 are lower than the peaks of JPC37, while the mass flux between the peak values clusters around 7 g/cm^2 kyr. During H1-3, the mass fluxes are around 20-30 g/cm^2 kyr. However, unlike JPC37, GVY001 shows a clearer signal of mass flux increase during Younger Dryas. The IRD flux from GVY001 ranges between 0 grains/cm^2 kyr and 190,000 grains/cm^2 kyr. It is the highest during H1 and H2 at or above 160,000 grains/cm^2 kyr, followed by the Last Glacial Maximum at 120,000 grains/cm^2 kyr, and H3 at 90,000 grains/cm^2 kyr. A "Student's" t-Test shows that the H3 IRD flux is distinctly different from the ambient sediment (p-value=1×10^{-10}).

5. Discussion

5.1. Interpretation of IRD flux

HE sedimentary layers have been viewed as the possible result of intervals of decreased foraminifera productivity, foraminifera dissolution, increased IRD deposition, or some combination of those influences (Broecker et al., 1992). Previously, the only $^{230}Th_{xs}$-based quantification of the depositional flux of grains that are uniquely identified as IRD during the HEs is from V28-82 in the eastern subpolar North Atlantic (McManus et al., 1998). The data from V28-82 showed that H1, H2, H4, and H5 were at least in part increased ice-rafting events, but left open the question for the two atypical events. Our new results from JPC37 and GVY001 reaffirm McManus et al.'s conclusion, showing increased IRD flux for the four most typical HEs (Fig. 4 c and Fig. 5). Additionally, here
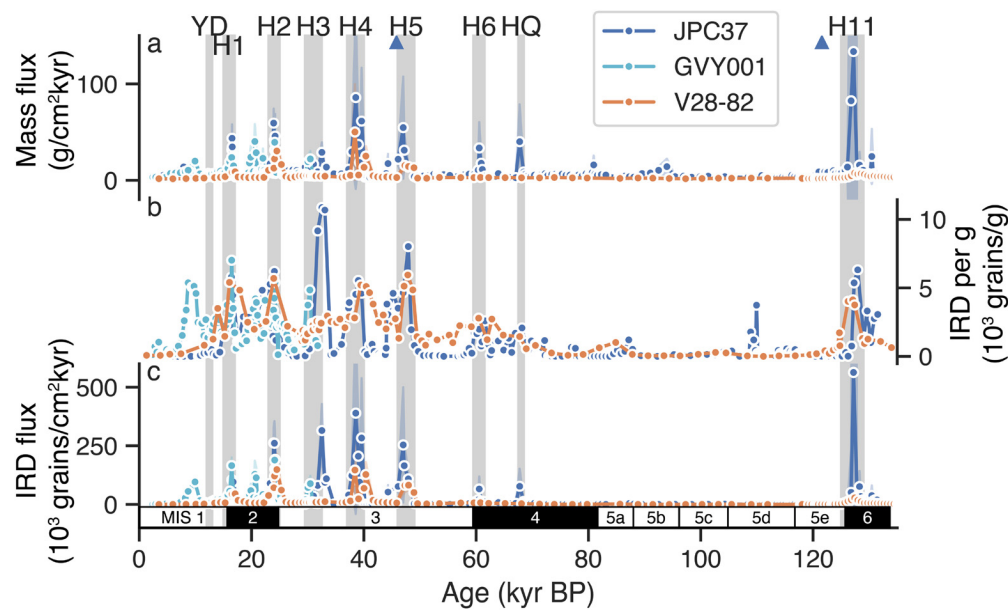
Fig. 4. Comparison of JPC37, GVY001, and V28-82 ^{230}Th$_{xs}$-normalized mass flux (a), IRD concentration (b), and IRD flux (c). Triangles in (a) are mass flux data points too high to quantify.
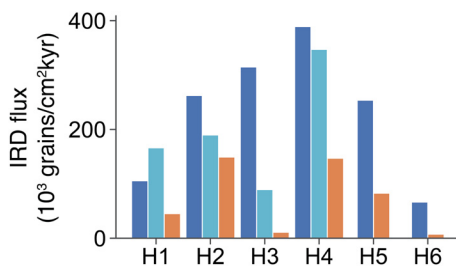
Fig. 5. Comparison of JPC37, GVY001, and V28-82 maximum IRD flux during HEs. See Fig. 4 for color legend. Note that no data is available from GVY001 during H5 and H6.

we show for the first time that, at least in the western North Atlantic, the sediment layers associated with H3 and H6 were also the result of increased ice-rafted deposition, rather than solely the result of reduced productivity near the sea surface or enhanced dissolution of foraminifera on the seafloor.

IRD fluxes in V28-82 are approximately half of those in both the western cores during H1 and H2, and about half of the IRD flux of JPC37 during H4 and H5 (Fig. 4c and Fig. 5). Even larger differences between IRD fluxes in the east and west are observed during H3, H6, and H11. The increases in IRD fluxes in V28-82 are muted during these events, whereas the IRD flux from JPC37 during H3 is thirty times higher than V28-82, during H6 nine times higher, and during H11 twenty times higher. Although H3 in JPC37 is near what may be a turbidite deposit, an increase in IRD flux during this interval also occurs in core GVY001, which has no evidence of turbidite deposition. At GVY001, the IRD flux during H3 is eight times higher than in V28-82. A comparison of IRD concentration and mass flux, two variables used to calculate IRD flux, reveals that much of the difference in IRD flux between V28-82 and the two western cores comes from the difference in mass flux. This comparison confirms that while IRD was an important sedimentary component at all three core locations, much more of it was deposited in the west than the east (Fig. 4 a and b). The IRD flux fills a gap at the western edge of the so-called Ruddiman belt. Ruddiman mapped the flux of sand-sized IRD in the North Atlantic during the MIS 2-4 and 5 but had no data from cores close to the

continental shelf (Ruddiman, 1977). Our data suggest a stronger zonal gradient in IRD flux than that suggested by Ruddiman.

Since the eastern core displays much lower IRD flux during H3 and H6, an even stronger zonal flux gradient may have existed during these two periods. The distinct melting patterns could be explained by any one or combination of the following factors: The calving flux from the Laurentide may have been smaller in magnitude during H3 and H6 so the majority of the drifting ice melted in the western NA without making it to the east; the released icebergs were "cleaner" and had lower concentrations of IRD; some different ice sheet(s) may have contributed to or dominated calving during this interval; or the melt rate of icebergs changed. We discuss the plausibility of each scenario below.

If the calving of icebergs from the Laurentide ice sheet increased during H3 and H6, but to a lesser extent than during the other events, the IRD fluxes associated with these two events would have displayed a visible but smaller increase than in the typical HEs across the subpolar Atlantic and a likely gradient from west to east. At face value, our data are consistent with this hypothesis. H3 and H6 do display increases in IRD flux that are smaller in magnitude than the other events, and there is a clear depositional gradient. Several hypotheses have been proposed to explain the smaller magnitude of calving during these events. Gwiazda et al. (1996) speculated that the ice sheet volume during H3 and H6 could have been smaller, leading to the smaller magnitude of calving. The logic of this inference follows from the observation that H3 and H6 occurred at the onset of the MIS 2 and 4, when the LIS was just starting to regrow after periods of warmth. This explanation does not work in the episodic surging framework since the LIS would have needed to reach a certain size before rapid calving occurred (Alley and MacAyeal, 1994 and references therein). Gwiazda et al.'s hypothesis may find support in research that shows a substantially reduced LIS during the MIS 3 (Dalton et al., 2019), although a later study cast doubt on that finding (Miller and Andrews, 2019). Contradicting Gwiazda et al., sea level was relatively low during H6 (Siddall et al., 2003). However, the exact contribution of the LIS to sea level change during this period remains unclear. A similar yet distinct hypothesis states that H4, which in our western cores appears to be a particularly large event, "gutted" the Hudson Strait, removing it of all ice (Kirby and Andrews, 1999). As a result, H3 occurred when the Laurentide was

still in a growth phase. However, a subsequent study suggested that Kirby and Andrews misidentified H3 (Rashid and Piper, 2007).

One intriguing possibility is that HEs were initiated by the repeated collapse of fringing ice shelves in the Labrador Sea (Hulbe et al., 2004). This collapse would have destabilized debris-laden ice streams that had previously been buttressed by the shelves, allowing them to advance rapidly and greatly increasing iceberg calving rates while decreasing the transport time of IRD from glacial incorporation to the open ocean. Instead of melting out below the shelf, much more of this IRD would then have been deposited across the Atlantic. In this case, one possible explanation for the limited IRD flux observed during H3 and H6 would then be an incomplete or short-lived ice-shelf collapse, thus limiting the number of icebergs subsequently discharged from advancing ice streams.

If the icebergs were loaded with less IRD content during the atypical events, the IRD fluxes could have decreased across the board compared to typical HEs, while maintaining a similar zonal gradient. Our data are also consistent with this scenario. IRD concentrations within icebergs may vary depending on the stage of ice stream purge (Alley and MacAyeal, 1994). The lack of a signal of H3 and H6 in V28-82 to the east might have reflected the greater distance from the source of icebergs, or the possibility that H3 and H6 icebergs were less dirty (e.g., Andrews and MacLean, 2003; Kirby and Andrews, 1999).

It has also been suggested that H3 and/or H6 may have had a European ice sheet origin (Bigg et al., 2011 and references therein). Our data do not support an entirely European origin for H3 and H6, since the deposition of IRD during each was demonstrably greater in the western North Atlantic. An iceberg trajectory model supports the unlikeliness of this scenario and suggests that the icebergs originating from the European ice sheet are mostly confined to the Norwegian Sea (Death et al., 2006). However, the IRD provenance study may still be valid because we cannot rule out that associated or precursor events of a European origin took place (Bigg et al., 2011).

An increased iceberg melt rate, caused by either warmer SST (Bond et al., 1992) and/or reduced sea ice cover (Wagner et al., 2018) could also have created a zonal IRD flux gradient. Our data do not directly support the hypothesis that warmer SST caused by a reorganization of hydrography or more intense iceberg ablation caused by a diminished sea ice extent led to more iceberg melting and deposition in the west during H3 and H6. Although IRD fluxes increased during H3 and H6 at our western sites, the fluxes are not higher than during the other HEs. Combined with the essential lack of increased IRD deposition at the eastern site, the total IRD flux during H3 and H6 appears to be lower compared to the other events.

IRD flux reconstruction provides a potentially important constraint on modeled iceberg discharge during HEs as a freshwater delivery mechanism (Death et al., 2006). While most HE modeling studies have focused on meltwater (Ganopolski and Rahmstorf, 2001; Meissner et al., 2002; Roche et al., 2004) and iceberg calving (Alvarez-Solas et al., 2013; Hulbe et al., 2004; Marshall and Koutnik, 2006), the absolute fluxes of meltwater and iceberg calving are challenging to reconstruct with paleo proxies. Meltwater proxies, including $\delta^{18}O$ (Cortijo et al., 1997), %C37:4 (Rodrigues et al., 2017), and $^{10}Be/^{9}Be$ (Valletta et al., 2018), while valuable, are currently only qualitative. IRD grain concentration can only provide a relative measure of the magnitude of iceberg calving (Bond et al., 1992). In contrast, IRD flux is a proxy that is both quantitative and accessible, with the potential for comparable model output. A better understanding of the IRD entrainment and delivery mechanisms could be developed by incorporating IRD fluxes into ice sheet calving simulations (Meyer et al., 2019). The direct data-model comparison of IRD flux can potentially help assess ice

sheet calving simulations and improve the understanding of calving behaviors (Levine and Bigg, 2008).

5.2. Sea surface proxies

The relative abundance of polar foraminifera (%*N. pachy.*) at GVY001 is saturated at 100% for most of the last glacial period, possibly due to the site's more poleward location (Fig. 3). The %*N. pachy.* data from JPC37 exhibit more variability, with increases during every HE layer, indicating repeated sea-surface cooling. During H1, H2, and H4, %*N. pachy.* seems to show a double-peaked structure. The double peaks might suggest that the SST is lowest at the beginning and end of these HEs but briefly returned to warmer temperatures midway through the events. We do not see a similar sequence of delayed onset in the deposition of IRD after the initial increase in *N. pachy.* abundance, as reported elsewhere (Barker et al., 2015).

The $\delta^{18}O$ of *N. pachy.* from JPC37 displays both the typical saw-tooth glacial-interglacial cycle and episodes of depletion associated with HEs (Fig. 3h). Since the increase in %*N. pachy.* during HEs implies a decrease in SST, the accompanying lower $\delta^{18}O$ in the same foraminifera cannot be the result of temperature changes. Instead, the likely explanation is that the melting icebergs released a large amount of $\delta^{18}O$-depleted freshwater during each HE. We do not observe this lowering of planktic $\delta^{18}O$ in H6 and HQ (discussed in the next section). Lower *N. pachy.* $\delta^{18}O$ during most HEs is consistent with previous studies on North Atlantic cores (Bond et al., 1992; Cortijo et al., 1997; Hillaire-Marcel et al., 1994), including the mapping of changes in *N. pachy.* $\delta^{18}O$ across the North Atlantic during H4 (Cortijo et al., 1997). The magnitude of changes observed in JPC37 during H4 ($\sim 1‰$) is comparable to a nearby core from that study (1.1‰ at SU90-11).

5.3. Extra events

The basis of our age model is partially the alignment of millennial-scale cooling events (C16-C24) identified throughout the North Atlantic region (McManus et al., 1994), including on the Iberian margin (Martrat et al., 2007; Greenland Stadials (GS) 17-25). An ice sheet modeling study predicted a previously unidentified HE that they named HQ during GS19, or C18 in the framework of the cooling events (Bassis et al., 2017). Our IRD flux from JPC37 provides the strongest evidence yet of the existence of HQ. There are two distinct IRD-flux events within C16 and C18. If the younger event is H6, consistent with an age of ~ 60 ka (Bassis et al., 2017; Hemming, 2004 and references therein; Martrat et al., 2007), it thus seems likely that the older event of the two is the hypothesized event HQ. Given that Bassis et al. identified H7b prior to HQ within C19, which we identified with our %*N. pachy.* record, it is unlikely that we mistake HQ for an earlier HE. These two IRD flux events also cannot be H5a (Rashid et al., 2003) since we found Ash Zone 2 at a shallower depth in the core. Ash Zone 2 is between H5a and H6, which gives us confidence with the designation of H6. We suggest that HQ and H6 may have been mistaken for one another in previous studies. Therefore, we recommend that ocean sediment studies that seek to identify H6 or HQ should have an accompanying SST proxy to resolve cooling events C16 and C18.

During the late last interglacial period at 70, 78, 87, 105, 109, and 117 ka, we found six additional IRD flux increases in JPC37 (Fig. S5). These IRD flux increases were two orders of magnitude smaller than HEs, and unlike the typical HEs, were not accompanied by coeval changes in Ca/Sr, magnetic susceptibility, density, %coarse, %IRD, and %*N. pachy.* Another difference relative to the HEs is that most of these interglacial IRD flux increases were preceded by discernable mass flux increases (Fig. S6). This repeated sequence

of events may give us a clue as to their origins. According to the turbidite-IRD sequence previously proposed to explain IRD layers in the Labrador Sea (Rashid et al., 2012), the early high mass flux could be caused by the initial meltwater discharge and the ensuing turbidity and nepheloid flow. This mechanism would increase mass flux without bringing in IRD. Following the turbidite facies, IRD would have been deposited as icebergs were discharged. The number of these locally high IRD flux events we identified corresponds to the number of cooling events during the last interglacial period proposed by McManus et al. (1994) (Fig. S7), which we tentatively marked in Fig. S5 and S6.

The lack of associated signals in other typical HE proxies (Fig. S5 and S6) during most of these cooling events raises questions about their nature. Among other explanations, the magnitude of the events could have been too small to have detectable changes in typical HE proxies. Alternatively, the source region of the delivered materials may have changed, which could have led to the muted responses in Ca/Sr and magnetic susceptibility. These events could also have been the result of meltwater outbursts, similar to the 8.2 ka event (Alley et al., 1997). A fourth potential explanation is that they were triggered by deep turbidity currents, as suggested by Hillaire-Marcel et al. (1994). Given that most of the events were associated with increases in %*N. pachy.*, it is unlikely that they were caused by the deep turbidity currents alone, although a combination of the above mechanisms is still possible.

6. Conclusions

(1) The IRD flux in the western North Atlantic cores JPC37 and GVY001 increased during each HE during the last glacial cycle. A single mechanism involving the LIS may therefore account for all HEs during this period.

(2) Compared to the only other available $^{230}Th_{xs}$-based IRD flux record, which is from the eastern North Atlantic, the western sites experienced much higher IRD flux during all HEs, notably including H3 and H6. We suggest that these two events, in the western North Atlantic at least, were the result of increased ice calving, rather than solely the result of other mechanisms such as increased foraminifera-dissolution or reduced productivity.

(3) IRD fluxes during H3 and H6 in the western North Atlantic are smaller than the other typical HEs. This result is most consistent with the hypothesis that the calving of icebergs from the LIS occurred during H3 and H6 but to a lesser extent than during the other events.

(4) All HEs were accompanied by surface cooling and all events except H6 and HQ saw freshening in the western subpolar North Atlantic.

(5) A series of previously identified cooling events during the MIS 5 interglacial were found in JPC37, accompanied by evidence for increased ice rafting that was two orders of magnitude smaller than HEs.

CRediT authorship contribution statement

Yuxin Zhou: Conceptualization, Investigation, Visualization, Writing – original draft, Writing – review & editing. **Jerry F. McManus:** Conceptualization, Funding acquisition, Project administration, Supervision, Writing – original draft, Writing – review & editing. **Allison W. Jacobel:** Investigation, Writing – review & editing. **Kassandra M. Costa:** Investigation, Writing – review & editing. **Shouyi Wang:** Investigation, Writing – review & editing. **Blanca Alvarez Caraveo:** Investigation, Writing – review & editing.

Declaration of competing interest

The authors declare that they have no known competing financial interests or personal relationships that could have appeared to influence the work reported in this paper.

Appendix A. Supplementary material

All data are archived in PANGAEA and can be accessed with this link: https://doi.org/10.1594/PANGAEA.911512.

Supplementary material related to this article can be found online at https://doi.org/10.1016/j.epsl.2021.116910.

References

Alley, R.B., MacAyeal, D.R., 1994. Ice-rafted debris associated with binge/purge oscillations of the Laurentide Ice Sheet. Paleoceanography 9, 503–511. https://doi.org/10.1029/94PA01008.

Alley, R.B., Mayewski, P.A., Sowers, T., Stuiver, M., Taylor, K.C., Clark, P.U., 1997. Holocene climatic instability: a prominent, widespread event 8200 yr ago. Geology 25, 483–486.

Alvarez-Solas, J., Robinson, A., Montoya, M., Ritz, C., 2013. Iceberg discharges of the last glacial period driven by oceanic circulation changes. Proc. Natl. Acad. Sci. USA 110, 16350–16354. https://doi.org/10.1073/pnas.1306622110.

Andersen, M.B., Stirling, C.H., Zimmermann, B., Halliday, A.N., 2010. Precise determination of the open ocean $^{234}U/^{238}U$ composition. Geochem. Geophys. Geosyst. 11. https://doi.org/10.1029/2010GC003318.

Andrews, J.T., 1998. Abrupt changes (Heinrich events) in late Quaternary North Atlantic marine environments: a history and review of data and concepts. J. Quat. Sci. 13, 3–16. https://doi.org/10.1002/(SICI)1099-1417(199801/02)13:1<3::AID-JQS361>3.0.CO;2-0.

Andrews, J.T., MacLean, B., 2003. Hudson strait ice streams: a review of stratigraphy, chronology and links with North Atlantic Heinrich events. Boreas 32, 4–17. https://doi.org/10.1080/03009480310001010.

Andrews, J.T., Voelker, A.H.L., 2018. "Heinrich events" (& sediments): a history of terminology and recommendations for future usage. Quat. Sci. Rev. 187, 31–40. https://doi.org/10.1016/j.quascirev.2018.03.017.

Bacon, M.P., Anderson, R.F., 1982. Distribution of thorium isotopes between dissolved and particulate forms in the deep sea. J. Geophys. Res. 87. https://doi.org/10.1029/JC087iC03p02045.

Barker, S., Chen, J., Gong, X., Jonkers, L., Knorr, G., Thornalley, D., 2015. Icebergs not the trigger for North Atlantic cold events. Nature 520, 333–336. https://doi.org/10.1038/nature14330.

Barnes, C.E., Cochran, J.K., 1990. Uranium removal in oceanic sediments and the oceanic U balance. Earth Planet. Sci. Lett. 97, 94–101. https://doi.org/10.1016/0012-821X(90)90101-3.

Bassis, J.N., Petersen, S.V., Mac Cathles, L., 2017. Heinrich events triggered by ocean forcing and modulated by isostatic adjustment. Nature 542, 332–334. https://doi.org/10.1038/nature21069.

Bigg, G.R., Levine, R.C., Green, C.L., 2011. Modelling abrupt glacial North Atlantic freshening: rates of change and their implications for Heinrich events. Glob. Planet. Change 79, 176–192. https://doi.org/10.1016/j.gloplacha.2010.11.001.

Bond, G., Heinrich, H., Broecker, W., Labeyrie, L., McManus, J., Andrews, J., Huon, S., Jantschik, R., Clasen, S., Simet, C., Tedesco, K., Klas, M., Bonani, G., Ivy, S., 1992. Evidence for massive discharges of icebergs into the North Atlantic Ocean during the last glacial period. Nature 360, 245–249. https://doi.org/10.1038/360245a0.

Broecker, W., Bond, G., Klas, M., Clark, E., McManus, J., 1992. Origin of the Northern Atlantic's Heinrich Events. Climate Dynamics, vol. 6, pp. 265–273.

Broecker, W.S., Andree, M., Bonani, G., Wolfli, W., Klas, M., Mix, A., Oeschger, H., 1988. Comparison between radiocarbon ages obtained on coexisting

planktonic foraminifera. Paleoceanography 3, 647–657. https://doi.org/10.1029/PA003i006p00647.

Chase, Z., Anderson, R.F., Fleisher, M.Q., Kubik, P.W., 2002. The influence of particle composition and particle flux on scavenging of Th, Pa and Be in the ocean. Earth Planet. Sci. Lett. 204, 215–229. https://doi.org/10.1016/S0012-821X(02)00984-6.

Cortijo, E., Labeyrie, L., Vidal, L., Vautravers, M., Chapman, M., Duplessy, J.-C., Elliot, M., Arnold, M., Turon, J.-L., Auffret, G., 1997. Changes in sea surface hydrology associated with Heinrich event 4 in the North Atlantic Ocean between 40° and 60°N. Earth Planet. Sci. Lett. 146, 29–45. https://doi.org/10.1016/S0012-821X(96)00217-8.

Costa, K.M., Hayes, C.M., Anderson, R.F., Pavia, F.J., Bausch, A., Deng, F., Dutay, J.-C., Geibert, W., Heinze, C., Henderson, G., Hillaire-Marcel, C., Hoffmann, S., Jaccard, S.L., Jacobel, A.W., Kienast, S.S., Lauren, K., Lerner, P., Lippold, J., Lund, D., Marcantonio, F., McGee, D., McManus, J.F., Mekik, F., Middleton, J.L., Missiaen, L., Not, C., Pichat, S., Robinson, L.F., Rowland, G.H., Roy-Barman, M., Tagliabue, A., Torfstein, A., Winckler, G., Zhou, Y., 2020. ^{230}Th normalization: New insights on an essential tool for quantifying sedimentary fluxes in the modern and Quaternary ocean. https://doi.org/10.1029/2019PA003820.

Dalton, A.S., Finkelstein, S.A., Forman, S.L., Barnett, P.J., Pico, T., Mitrovica, J.X., 2019. Was the Laurentide Ice Sheet significantly reduced during marine isotope stage 3? Geology 47, 111–114. https://doi.org/10.1130/G45335.1.

Dansgaard, W., Johnsen, S.J., Clausen, H.B., Dahl-Jensen, D., Gundestrup, N.S., Hammer, C.U., Hvidberg, C.S., Steffensen, J.P., Sveinbjörnsdóttir, A.E., Jouzel, J., Bond, G.C., Sveinbjörnsdottir, A.E., Jouzel, J., Bond, G.C., 1993. Evidence for general instability of past climate from a 250-kyr ice-core record. Nature 364, 218–220. https://doi.org/10.1038/364218a0.

Death, R., Siegert, M.J., Bigg, G.R., Wadley, M.R., 2006. Modelling iceberg trajectories, sedimentation rates and meltwater input to the ocean from the Eurasian Ice Sheet at the last glacial maximum. Palaeogeogr. Palaeoclimatol. Palaeoecol. 236, 135–150. https://doi.org/10.1016/j.palaeo.2005.11.040.

Ehlers, J., Ehlers, Jürgen, Gibbard, P.L., Hughes, P.D., 2011. Quaternary Glaciations - Extent and Chronology: A Closer Look. Elsevier.

EPICA Community Members, 2006. One-to-one coupling of glacial climate variability in Greenland and Antarctica. Nature 444, 195–198. https://doi.org/10.1038/nature05301.

EPICA Community Members, 2004. Eight glacial cycles from an Antarctic ice core. Nature 429, 623–628. https://doi.org/10.1038/nature02599.

Ericson, D.B., 1959. Coiling direction of Globigerina pachyderma as a climatic index. Science 130, 219–220.

Fleisher, M.Q., Anderson, R.F., 1991. Particulate matter digestion and radionuclide blanks. Geophys. Monogr. 63, 221–222.

Ganopolski, A., Rahmstorf, S., 2001. Rapid changes of glacial climate simulated in a coupled climate model. Nature 409, 153–158. https://doi.org/10.1038/35051500.

Gwiazda, R.H., Hemming, S.R., Broecker, W.S., 1996. Provenance of icebergs during Heinrich event 3 and the contrast to their sources during other Heinrich episodes. Paleoceanography 11, 371–378. https://doi.org/10.1029/96PA01022.

Heaton, T.J., Köhler, P., Butzin, M., Bard, E., Reimer, R.W., Austin, W.E.N., Bronk Ramsey, C., Grootes, P.M., Hughen, K.A., Kromer, B., Reimer, P.J., Adkins, J., Burke, A., Cook, M.S., Olsen, J., Skinner, L.C., 2020. Marine20—the marine radiocarbon age calibration curve (0–55, 000 cal BP). Radiocarbon 62, 779–820. https://doi.org/10.1017/RDC.2020.68.

Hemming, S.R., 2004. Heinrich events: massive late Pleistocene detritus layers of the North Atlantic and their global climate imprint. Rev. Geophys. 42, 1–43. https://doi.org/10.1029/2003RG000128.

Hemming, S.R., Hall, C.M., Biscaye, P.E., Higgins, S.M., Bond, G.C., McManus, J.F., Barber, D.C., Andrews, J.T., Broecker, W.S., 2002. ^{40}Ar/^{39}Ar ages and ^{40}Ar * concentrations of fine-grained sediment fractions from North Atlantic Heinrich layers. Chem. Geol. 182, 583–603. https://doi.org/10.1016/S0009-2541(01)00342-4.

Hendry, K.R., Huvenne, V.A.I., Robinson, L.F., Annett, A., Badger, M., Jacobel, A.W., Ng, H.C., Opher, J., Pickering, R.A., Taylor, M.L., Bates, S.L., Cooper, A., Cushman, G.G., Goodwin, C., Hoy, S., Rowland, G., Samperiz, A., Williams, J.A., Achterberg, E.P., Arrowsmith, C., Alexander Brearley, J., Henley, S.F., Krause, J.W., Leng, M.J., Li, T., McManus, J.F., Meredith, M.P., Perkins, R., Woodward, E.M.S., 2019. The biogeochemical impact of glacial meltwater from Southwest Greenland. Prog. Oceanogr. 176, 102126. https://doi.org/10.1016/j.pocean.2019.102126.

Henry, L.G., McManus, J.F., Curry, W.B., Roberts, N.L., Piotrowski, A.M., Keigwin, L.D., 2016. North Atlantic Ocean circulation and abrupt climate change during the last glaciation. Science 353, 470–474. https://doi.org/10.1126/science.aaf5529.

Hesse, R., 2016. Ice-proximal Labrador Sea Heinrich layers: a sedimentological approach. Can. J. Earth Sci. 53, 71–100. https://doi.org/10.1139/cjes-2015-0033.

Hillaire-Marcel, C., Vernal, A., de Bilodeau, G., Wu, G., 1994. Isotope stratigraphy, sedimentation rates, deep circulation, and carbonate events in the Labrador Sea during the last ~200 ka. Can. J. Earth Sci. 31, 63–89. https://doi.org/10.1139/e94-007.

Hodell, D.A., Channeil, J.E.T., Curtis, J.H., Romero, O.E., Röhl, U., 2008. Onset of "Hudson Strait" Heinrich events in the eastern North Atlantic at the end of the middle Pleistocene transition (~640 ka)? Paleoceanography 23, 1–16. https://doi.org/10.1029/2008PA001591.

Hughen, K., Lehman, S., Southon, J., Overpeck, J., Marchal, O., Herring, C., Turnbull, J., 2004. 14C activity and global carbon cycle changes over the past 50,000 years. Science 303, 202–207. https://doi.org/10.1126/science.1090300.

Hulbe, C.L., MacAyeal, D.R., Denton, G.H., Kleman, J., Lowell, T.V., 2004. Catastrophic ice shelf breakup as the source of Heinrich event icebergs. Paleoceanography 19, PA1004. https://doi.org/10.1029/2003PA000890.

Jullien, E., Grousset, F.E., Hemming, S.R., Peck, V.L., Hall, I.R., Jeantet, C., Billy, I., 2006. Contrasting conditions preceding MIS3 and MIS2 Heinrich events. Glob. Planet. Change 54, 225–238. https://doi.org/10.1016/j.gloplacha.2006.06.021.

Kirby, E., Andrews, T., 1999. Mid-Wisconsin Laurentide Ice Sheet growth and decay: implications for Heinrich events 3 and 4. Paleoceanography 14, 211–223.

Levine, R.C., Bigg, G.R., 2008. Sensitivity of the glacial ocean to Heinrich events from different iceberg sources, as modeled by a coupled atmosphere-iceberg-ocean model. Paleoceanography 23, 1–16. https://doi.org/10.1029/2008PA001613.

Marshall, S.J., Koutnik, M.R., 2006. Ice sheet action versus reaction: distinguishing between Heinrich events and Dansgaard-Oeschger cycles in the North Atlantic. Paleoceanography 21, 1–13. https://doi.org/10.1029/2005PA001247.

Martrat, B., Grimalt, J.O., Shackleton, N.J., de Abreu, L., Hutterli, M.A., Stocker, T.F., 2007. Four climate cycles of recurring deep and surface water destabilizations on the Iberian margin. Science 317, 502–507. https://doi.org/10.1126/science.1139994.

McCartney, M., 1992. Recirculating components to the deep boundary current of the northern North Atlantic. Prog. Oceanogr. 29, 283–383.

McManus, J.F., Anderson, R.F., Broecker, W.S., Fleisher, M.Q., Higgins, S.M., 1998. Radiometrically determined sedimentary fluxes in the sub-polar North Atlantic during the last 140,000 years. Earth Planet. Sci. Lett. 155, 29–43. https://doi.org/10.1016/S0012-821X(97)00201-X.

McManus, J.F., Bond, G.C., Broecker, W.S., Johnsen, S., Labeyrie, L., Higgins, S., 1994. High-resolution climate records from the North Atlantic during the last interglacial. Nature 371, 326–329. https://doi.org/10.1038/371326a0.

McManus, J.F., Francois, R., Gherardl, J.M., Kelgwin, L., Drown-Leger, S., 2004. Collapse and rapid resumption of Atlantic meridional circulation linked to deglacial climate changes. Nature 428, 834–837. https://doi.org/10.1038/nature02494.

McManus, J.F., Oppo, D.W., Keigwin, L.D., Cullen, J.L., Bond, G.C., 2002. Thermohaline circulation and prolonged interglacial warmth in the North Atlantic. Quat. Res. 58, 17–21. https://doi.org/10.1006/qres.2002.2367.

Meissner, K.J., Schmittner, A., Wiebe, E.C., Weaver, A.J., 2002. Simulations of Heinrich events in a coupled ocean-atmosphere-sea ice model: simulations of Heinrich events. Geophys. Res. Lett. 29, 16-1-16–3. https://doi.org/10.1029/2001GL013514.

Meyer, C.R., Robel, A.A., Rempel, A.W., 2019. Frozen fringe explains sediment freeze-on during Heinrich events. Earth Planet. Sci. Lett. 524, 115725. https://doi.org/10.1016/j.epsl.2019.115725.

Miller, G.H., Andrews, J.T., 2019. Hudson Bay was not deglaciated during MIS-3. Quat. Sci. Rev. 225, 105944. https://doi.org/10.1016/j.quascirev.2019.105944.

Murray, R.W., Miller, D.J., Kryc, K.A., 2000. Analysis of major and trace elements in rocks, sediments, and interstitial waters by inductively coupled plasma-atomic emission spectrometry (ICP-AES). ODP Tech. Note.

NGRIP members, 2004. High-resolution record of Northern Hemisphere climate extending into the last interglacial period. Nature 431, 147–151. https://doi.org/10.1038/nature02805.

Rashid, H., Hesse, R., Piper, D.J.W., 2003. Evidence for an additional Heinrich event between H5 and H6 in the Labrador Sea. Paleoceanography 18, 1–15. https://doi.org/10.1029/2003PA000913.

Rashid, H., Piper, D.J., 2007. The extent of ice on the continental shelf off Hudson Strait during Heinrich events 1-3. Can. J. Earth Sci. 44, 1537–1549. https://doi.org/10.1139/e07-051.

Rashid, H., Saint-Ange, F., Barber, D.C., Smith, M.E., Devalia, N., 2012. Fine scale sediment structure and geochemical signature between eastern and western North Atlantic during Heinrich events 1 and 2. Quat. Sci. Rev. 46, 136–150. https://doi.org/10.1016/j.quascirev.2012.04.026.

Robinson, L.F., Noble, T.L., McManus, J.F., 2008. Measurement of adsorbed and total ^{232}Th/^{230}Th ratios from marine sediments. Chem. Geol. 252, 169–179. https://doi.org/10.1016/j.chemgeo.2008.02.015.

Roche, D., Paillard, D., Cortijo, E., 2004. Constraints on the duration and freshwater release of Heinrich event 4 through isotope modelling. Nature 432, 379–382. https://doi.org/10.1038/nature03059.

Rodrigues, T., Alonso-García, M., Hodell, D.A., Rufino, M., Naughton, F., Grimalt, J.O., Voelker, A.H.L., Abrantes, F., 2017. A 1-Ma record of sea surface temperature and extreme cooling events in the North Atlantic: a perspective from the Iberian margin. Quat. Sci. Rev. 172, 118–130. https://doi.org/10.1016/j.quascirev.2017.07.004.

Ruddiman, W.F., 1977. North Atlantic ice-rafting: a major change at 75,000 years before the present, vol. 196. Science 196, 1208–1211. https://doi.org/10.1126/science.196.4295.1208.

Ruddiman, W.F., Glover, L.K., 1972. Vertical mixing of ice-rafted volcanic ash in North Atlantic sediments. Geol. Soc. Am. Bull. 83, 2817–2836.

Siddall, M., Rohling, E., Almogi-Labin, A., Hemleben, C., Meischner, D., Schmelzer, I., Smeed, D.A., 2003. Sea-level fluctuations during the last glacial cycle. Nature 423, 853–858. https://doi.org/10.1038/nature01687.1.

Southon, J., 2004. A radiocarbon perspective on Greenland ice-core chronologies: can we use ice cores for ^{14}C calibration? Radiocarbon 46, 1239–1259. https://doi.org/10.1017/S0033822200033129.

Stockli, R., Vermote, E., Saleous, N., Simmon, R., Herring, D., 2005. The Blue Marble Next Generation - a true color Earth dataset including seasonal dynamics from MODIS.

Stuiver, M., Reimer, P.J., Reimer, R.W., 2021. CALIB 8.2. [WWW program].

Svensson, A., Andersen, K.K., Bigler, M., Clausen, H.B., Dahl-Jensen, D., Davies, S.M., Johnsen, S.J., Muscheler, R., Parrenin, F., Rasmussen, S.O., Röthlisberger, R., Seierstad, I., Steffensen, J.P., Vinther, B.M., 2008. A 60 000 year Greenland stratigraphic ice core chronology. Clim. Past 4, 47–57. https://doi.org/10.5194/cp-4-47-2008.

Valletta, R.D., Willenbring, J.K., Passchier, S., Elmi, C., 2018. [10]Be/[9]Be ratios reflect Antarctic ice sheet freshwater discharge during Pliocene warming. Paleoceanogr. Paleoclimatol. https://doi.org/10.1029/2017PA003283.

Wagner, T.J.W., Dell, R.W., Eisenman, I., Keeling, R.F., Padman, L., Severinghaus, J.P., 2018. Wave inhibition by sea ice enables trans-Atlantic ice rafting of debris during Heinrich events. Earth Planet. Sci. Lett. 495, 157–163. https://doi.org/10.1016/j.epsl.2018.05.006.